NUMERICAL STUDY ON AERODYNAMIC PERFORMANCE AND PARTICLE EROSION CHARACTERISTICS OF FLUE GAS TURBINE

by

Liuxi CAI[a], Jiawei YAO[a], Yanfang HOU[a], Yun LI[a*], Shunsen WANG[b], and Jingru MAO[b]

[a] School of Chemical Engineering and Technology, Xi'an Jiaotong University, Xi'an, China
[b] State Key Laboratory of Multi-phase Flow in Power Engineering, Xi'an Jiaotong University, Xi'an, China

Original scientific paper
https://doi.org/10.2298/TSCI221125072C

The 3-D numerical simulation method is coupled with erosion and particle rebound models based on the results of high temperature erosion tests to systematically study the gas-solid two-phase flow characteristics of a flue gas turbine for the first time. The aerodynamic loss characteristics of the flue gas-steam mixtures and particle erosion mechanism in the flue gas turbine cascade under design and non-design conditions are investigated. The results indicate that the mixing loss of cooling steam and gas, secondary flow loss, and separation loss significantly affect the entropy increment of the rotor cascade. The isentropic efficiency of the flue gas turbine under the design condition is 78.74%. The radial inflow of wheel cooling steam from the axial clearance has a radial impact and mixing effect on the mainstream flue gas, enhancing the generation and development of the secondary flow vortex in the rotor cascade. When the dimensionless cooling steam flow rate is reduced from 1 to 0.6, the isentropic efficiency of the flue gas turbine increases by approximately 0.9%. By contrast, when the dimensionless cooling steam flow rate increases from 1 to 2, the isentropic efficiency decreases by 0.42%. The erosion rate of the leading and trailing edges of the rotor is higher than those at other streamwise locations. The erosion of the rotor leading edge and the blade-tip trailing edge is caused by the high speed impact of particles above 10 μm, while the erosion of the rotor root is caused by the grinding of 1-5 μm particles carried by the secondary flow.

Key words*: flue gas, aerodynamic performance, entropy increment, erosion damage, numerical simulation*

Introduction

The flue gas turbine is a key equipment for flue gas heat recovery systems in catalytic cracking, nitric acid, and coal gasification units in refineries and other process applications. During operation, regenerated flue gas is separated from catalyst particles using a three-stage cyclone separator and then fed into the flue gas turbine to expand and perform work, thereby driving the main fan or directly driving the generator to allow the recovery of heat and pressure energy of regenerated flue gas [1, 2]. During the process, superheated steam with a lower temperature is typically introduced in the front and rear wheel of the flue gas turbine to cool the wheel and rotor parts of the turbine, which complicates the flow in the turbine cascade and

* Corresponding author, e-mail: yunli@mail.xjtu.edu.cn

causes flow losses. In addition, because the regenerated flue gas contains a large quantity of hard catalyst particles, a significant number of particles enter the flue gas turbine with the flue gas, causing severe erosion damage to the flue gas turbine blades [3, 4]. The particle erosion can change the roughness and profile of the blade cascade, which reduces the aerodynamic efficiency of the flue gas turbine [5, 6]. In extreme cases, it results in local stress concentration in the blade and causes accidents such as blade fracture [7, 8].

To mitigate catalyst particle erosion and corrosion on flue gas turbine blades, original equipment manufacture (OEM) typically spray anti-wear coatings on the blade cascade surfaces. Sun *et al.* [9] found that the co-base alloy coating prepared via plasma spraying and ceramic coating prepared via explosive spraying were effective for extending the service life of flue gas turbine blades. However, a systematic experimental study by Min *et al.* [10], Liu [11], and Cai *et al.* [12] revealed that the anti-wear performance of thermally sprayed coatings derived from different spraying process varied significantly. For extending the efficient service life of flue gas turbines, researchers have employed CFD to optimize the blade channel structure of the turbines and reduce the intensity of blade erosion [13]. Maceli *et al.* [1] analyzed single-stage flue gas turbines via numerical simulations. They determined that the particles entering the rotating blade erode the leading edge of the rotating blade suction surface and the pressure surface near the trailing edge. Carbonetto *et al.* [14] performed a 3-D numerical simulation optimize the inlet runner structure and blade profile, and the service life of the blade was increased by 50-100%. Du *et al.* [15, 16] conducted gas-solid two-phase flow simulation and found that particles larger than 20 μm are likely to cause scouring and wearing of the blades. The numerical studies of Gandhi *et al.* [17] indicated that the leading edge of the rotating blade is susceptible to particle impingement, resulting in erosion. Liu *et al.* [4] demonstrated that catalyst particles accelerated by the stator cascade impinge on the leading and trailing edges of the rotor blade and the erosion of the leading edge is more severe than that of the trailing edge.

Several studies have focused on determining the aerodynamic characteristics and particle erosion behavior of flue gas turbines via numerical simulation methods, however, the actual structure and working fluid of flue gas turbines were simplified in almost all the aforementioned studies. In addition, the effects of the wheel cooling steam on the aerodynamic performance and particle erosion behavior of flue gas turbines were not considered. To address these limitations, the 3-D numerical simulation method coupled with erosion and particle rebound models based on the results of high temperature erosion tests were employed in this study to systematically investigate the gas-solid two-phase flow characteristics of a flue gas turbine for the first time. The aerodynamic loss characteristics of the flue gas-steam mixtures and particle erosion mechanism in the flue gas turbine cascade under design and non-design conditions were elucidated, providing a technical basis for efficient blade profile design and safe operation of the flue gas turbine.

Geometric model and numerical approach

Geometric model

The flue gas turbine considered in this study is designed for use in a petroleum refinery, and its geometric model is presented in fig. 1. The single-stage flue gas turbine has an axial inlet cantilever rotor structure, an inlet pressure of 0.29 MPa, an inlet temperature of 943 K, a flue gas-flow rate of 635 Nm^3 per minute, an exhaust pressure of 0.097 MPa, and a rotational speed of 6915 rpm. The diameter of the regeneration flue gas inlet pipe is 850 mm, and the radius of the rotor hub is 350 mm. The aerodynamic installation angles of the stator and rotating blade are 30° and 65°, respectively. Owing to the high temperature of the flue gas medium, in

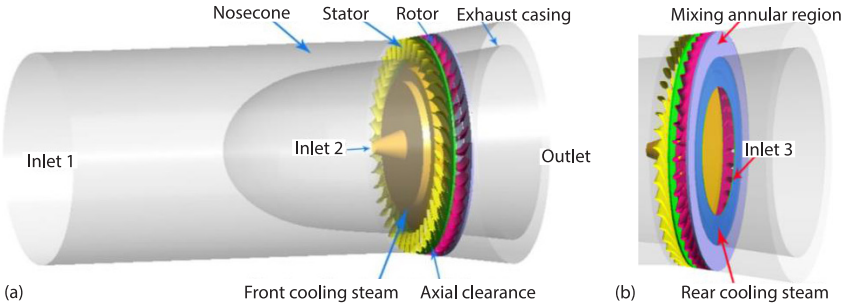

Figure 1. Geometric model and sub-fluid domain;
(a) view from the gas admission side and (b) view form the exhaust side

addition the use of alloy materials with good resistance to high temperatures, the flue gas turbine wheel is typically equipped with front and rear steam cooling, as shown in fig. 1, to reduce the thermal stress and surface temperature of the high temperature components and ensure that the working temperature of the wheel is within the range of 573-623 K. The front cooling steam (*i.e.*, wheel cooling steam) is introduced into the casing through the pipe-line, injected via the horn to the center of the wheel, and flows radially along the front surface of the wheel to cool it, and finally flows into the axial clearance. Rear cooling steam (*i.e.*, the shaft end sealing steam behind the wheel) enters the casing, flows radially along the rear side of the wheel to cool it, and finally flows into the mixing annular region downstream of the rotating blade through the end surface of the wheel.

The computational model used in this study considers the entire fluid domain of the flue gas turbine, as shown in fig. 1. To achieve the research objectives, the fluid domain of the flue gas turbine was divided into eight sub-calculation regions: the nosecone, stator cascade, axial clearance between the stators and rotating blades, rotor cascade, mixing annular region, exhaust casing, front cooling steam fluid domain (front side of the turbine wheel), and rear cooling steam (shaft end sealing) fluid domain.

Numerical methods

The time-averaged continuity, momentum, and energy equations of the 3-D steady-state viscous flow in the cascade channel were obtained from the relevant literature [18, 19]. Considering that the working fluids of flue gas turbines are multicomponent mixtures, the overall average value of the fluid parameters for multicomponent fluids must be introduced for the solution of the control equations. Specifically, the effects of different components are introduced by altering the overall average value. In addition, each component must ensure mass conservation and reflect the flow conditions inside the fluid mixture.

The Reynolds average mass equation for each component can be expressed:

$$\frac{\partial \tilde{\rho}_i}{\partial t} + \frac{\partial\left(\tilde{\rho}_i \tilde{U}_j\right)}{\partial x_j} = -\frac{\partial}{\partial x_j}\left(\rho_i\left(\tilde{U}_{ij} - \tilde{U}_j\right) - \overline{\rho_i'' U_j''}\right) + S_i \tag{1}$$

where $\tilde{\rho}_i$ is the mass-average density of fluid component i in the mixture,

$$\tilde{U}_j = \sum \frac{\rho_i \tilde{U}_{ij}}{\bar{\rho}}$$

represents the mass-average velocity, $\tilde{U}_{ij}$ is the mass-average velocity of component i, $\rho_i(\tilde{U}_{ij} - \tilde{U}_j)$ represents the relative mass-flow rate, and S_i is the source term of component i including chemical reaction factors.

The sum of mass fractions of all components of the working medium is 1. To ensure the mass conservation of the mixed fluid, only $N - 1$ mass equations were solved in CFX-Solver, and the remaining component was set as the control component. This control component was determined using the constraint equation:

$$\sum_{i=1,2,3...}^{N} Y_i = 1 \tag{2}$$

where Y_i is the mass fraction of each component. The basic physical parameters of any fluid can be derived from the equation:

$$\alpha = \sum_{i=1,2,3...}^{N} Y_i \alpha_i \tag{3}$$

where α_i is an arbitrary physical parameter of fluid component i.

In CFX-Solver, the diffusion coefficient, enthalpy, and mass fraction of the components are average values. Therefore, the supplementary energy equation takes the form:

$$\frac{\partial}{\partial t}(\rho H) - \frac{\partial P}{\partial t} + \frac{\partial}{\partial x_i}(\rho U_j H) = \frac{\partial}{\partial x_j}\left(\lambda \frac{\partial T}{\partial x_j} + \sum_{i=1,2,3...}^{N_c} \Gamma_i h_i \frac{\partial Y_i}{\partial x_j} + \frac{\mu_t}{\mathrm{Pr}_t}\frac{\partial h}{\partial x_j}\right) + S_E \tag{4}$$

Because the SST k-ω turbulence model combines the excellent performance of the standard k-ω turbulence model within the boundary-layer and the advantages of the k-ε turbulence model in the bulk flow region and considers the transfer of shear stress, it is effective for predicting the flow in the presence of boundary-layer separation. In this study, the SST k-ω turbulence model, auto wall function, and gamma theta transition model were used to simulate the flow process of flue gas in the flow passages of the flue gas turbine.

In the calculation, the effects of the Stokes drag force, gravity, rotational force, turbulent diffusion force, and pressure-gradient force on the particles were considered, and the Schiller-Naumann drag model was used to model the Stokes drag force. A stochastic approach was adopted in the particle-phase control equation determine the instantaneous velocity of the fluid, and the discrete random walk model was introduced. The relationship between the particle and continuous phases when the discrete vortex was continuously generated and extinguished was considered.

To mitigate the influence of grid density on the calculation results, four sets of grids were used to discretize the model fluid domain, and the grid numbers were $1.3 \cdot 10^7$, $1.75 \cdot 10^7$, $2.2 \cdot 10^7$, and $2.7 \cdot 10^7$. Table 1 lists the flue gas turbine flow Q_m, outlet flue gas temperature, and maximum velocity of 10 μm particles for the different grid numbers. Evidently, when the grid number exceeds $1.75 \cdot 10^7$, the flue gas turbine flow becomes more stable with an increase in the grid number, and the variations in the outlet flue gas temperature and the maximum velocity of 10 μm particles were smaller than 0.052% and 0.04%, respectively. This suggests that when the grid number reaches $1.75 \cdot 10^7$, the effects of the grid number on the aerodynamic performance of the flue gas turbine and the blade erosion characteristics considered in this study become negligible. To improve the simulation accuracy, a grid number greater than $2.2 \cdot 10^7$ was used in the fluid calculation domain, and the grid of a representative region is shown in fig. 2. In addition, the error between the simulation results for the flue gas outlet tem-

perature listed in tab. 1 and the test values of the exhaust gas temperature from OEM under the design conditions was only 0.1%, confirming the reliability of the numerical simulation method employed in this study.

Table 1. Grid sensitivity test

Grid number	Q_{mg} [kgs^{-1}]	T_{out} [kgs^{-1}]	$V_{10\mu m}$ [ms^{-1}]
$1.3 \cdot 10^7$	15.137	771.4	474.30
$1.75 \cdot 10^7$	15.136	770.3	471.88
$2.2 \cdot 107$	15.136	769.9	471.93
$2.7 \cdot 107$	15.136	769.6	471.74

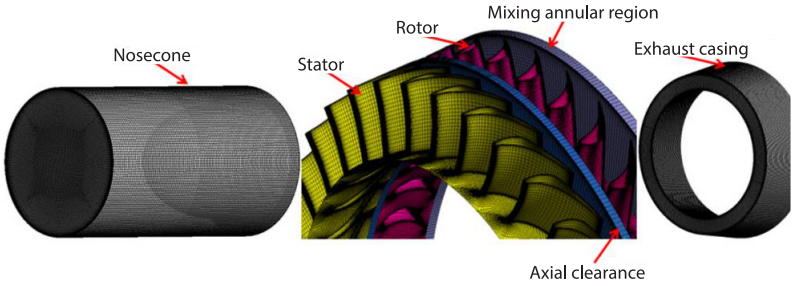

Figure 2. Grid in typical regions

Boundary conditions

The regenerated flue gas at the inlet of the flue gas turbine is a mixture of several gases, including N_2 (volume fraction 74%), CO_2 (13.72%), O_2 (2.76%), SO_2 (0.01%), and superheated steam (9.51%). The medium for cooling the wheel through the front and rear domains is superheated steam. In defining the fluid medium, a mixture of fixed composition, corresponding to the regenerated flue gas at the inlet of the inflow nosecone (with the aforementioned composition), was defined first, and each monomeric gas was selected from the gas phase combustion database, following the ideal gas equation of state. In the second step, a pure-substance superheated steam was defined, corresponding to the turbine cooling and sealing steam. In the third step, a variable composition mixture of regenerated flue gas and turbine cooling steam was defined, which was adopted to describe the fluid properties in the mixing region of the flue gas and cooling steam.

The total pressure and temperature conditions of the regenerated flue gas were set at the inlet of the turbine (Inlet 1). The static pressure condition was set at the outlet of the turbine. Inlets 2 and 3 (corresponding to the front and rear cooling steam domains, respectively) were set as mass-flow inlets with steam flow rates of 0.139 kg/s and 0.05556 kg/s, respectively, and a steam temperature of 523 K. To match the actual service environment as closely as possible, a fixed temperature of 598 K was set for the surface of the wheel, and the adiabatic condition was assumed at the other solid walls. The inlet turbulence intensity was set as 5%, and the stage (mixing plane) model was adopted for the data transfer between the nosecone and stators and the interface between the stators and rotating blades.

According to the HG/T3650-2012 standard of China, the dust concentration of flue gas entering the flue gas turbine should be lower than 200 mg/Nm^3 after the flue gas passes through the three-stage cyclone de-dusting, and the proportion of particles larger than 10 μm

in the flue gas should be less than 3%. However, in previous studies [5, 20, 21], the proportion of catalyst particles larger than 10 μm in the flue gas turbine was typically 15% owing to the poor particle separation performance of the cyclone separator. The particle-size distribution is listed in tab. 2. Considering a flue gas turbine inlet volume of 635 Nm^3 per minute and particle concentration of 200 mg/Nm^3, the total particle flow rate was set as 2 g/s.

Table 2. Particle-size distribution at the inlet of the nosecone

Particle size [μm]	Volume fraction	Representative diameters [μm]	Particle concentration [g^{s-1}]
≤10	85%	1, 5, and 10	1.7
10-20	10%	15 and 20	0.2
20-40	5%	30	0.1

To comprehensively investigate the motion and erosion behavior of particles with different sizes in the cascade of the flue gas turbine, a total of six mono-size particles were set in the inlet of the nosecone, corresponding to different particle-size bands. The concentrations of each particle size are listed in tab. 2. Considering that the catalyst particles flow through a long flue gas pipe-line before entering the nosecone of the flue gas turbine, they are fully mixed with and accelerated by the flue gas. Therefore, a slip velocity of zero was set for the particles at the flue gas inlet, and the particle positions were assumed to be uniformly distributed. Numerous studies have indicated [6, 22, 23] that the microscopic shape of catalyst particles is nearly spherical and that they are primarily composed of SiO_2 and Al_2O_3, which account for over 90%. Therefore, the discrete particle properties were set according to SiO_2 with a density of 2650 kgm^{-3}, and the shape factor was set as 1.0 for catalyst particles of different sizes.

Erosion and particle rebound models

Considering that the catalyst particles are mainly composed of SiO_2 and Al_2O_3 and that the walls of the flow passages of flue gas turbines are typically sprayed with ceramic coatings such as Cr_3C_2-NiCr, the rebound model was selected for quartz sand particles impinging on the brittle coating to describe the rebound behavior of the particles. Details of the experiment are presented in a previous study [24]. The uncertainties in the particle velocity magnitude and direction measured using particle image velocimetry in the experiments were below 2% and 1°, respectively. The least-squares method was used to fit the experimental results for the particle incidence velocity, rebound velocity, and particle incidence angle and obtain the expressions of the tangential velocity recovery coefficient e_T and normal velocity recovery coefficient e_N for quartz sand particles impacting the coating material:

$$e_T = 1.0011 - 0.0957\beta - 1.1458\beta^2 + 1.8356\beta^3 - 0.6797\beta^4 \tag{5}$$

$$e_N = 0.997 - 5.1006\beta + 11.134\beta^2 - 9.5664\beta^3 + 2.7629\beta^4 \tag{6}$$

where β is the angle of particle incidence. The particle erosion was modeled using the hard particle impact explosive spraying Cr_3C_2 coating [25] at high temperature and is expressed:

$$\begin{aligned} E_m &= A_T(T)B(\beta)V^{n(\beta)} \\ A_T(T) &= 8.429 - 0.0085T \end{aligned} \tag{7}$$

$$\begin{aligned} B(\beta) &= -0.0001 + 0.222\beta - 0.362\beta^2 + 0.232\beta^3 0 - .052\beta^4 \\ n(\beta) &= 1.522 + 2.786\beta - 0.876\beta^2 \end{aligned} \tag{8}$$

where T and V are the erosion ambient temperature and particle impact velocity, respectively.

Results and discussion

Aerodynamic loss analysis of the flue gas turbine under design conditions

Figure 3 shows the contours of the flue gas-flow field at the midspan. According to the working principle of the flue gas turbine, the flue gas will initially accelerate when it flows through the nosecone. After entering the stator cascade of the flue gas turbine, the flue gas further expanded and accelerated. Considering the flow passages for the stators had a Laval nozzle shape, the flue gas reached the critical state (Ma = 1) when flowing through the throat of the stator cascade, after which it expanded further, and the pressure and temperature continued to decrease. Finally, the flue gas velocity reached the supersonic state, with a Mach number exceeding 1.5. Owing to the excessive expansion of the flue gas at the stator cascade, the pressure difference between the nozzle cascade and the downstream region induced a shockwave at the exit of the stator cascade. The shockwave resulted in an increase in both the flue gas pressure and temperature, and the Mach number of the flue gas gradually decreased to less than 1.0. As is evident from fig. 3(c), the boundary-layer of the stator surface-particularly on the suction surface-exhibits a tendency to thicken before and after the shockwave, and the frictional loss of the boundary-layer increases. In addition, the flue gas enters the flow passages of rotating blades at a positive attack angle, resulting in a local air-flow separation at the blade suction surface when the gas-flows through the turning position of the rotor cascade, resulting in gas separation loss.

Figure 3. Contours of the flue gas temperature, pressure, and Mach number at the midspan; (a) temperature, (b) pressure, and (c) Mach number

Figure 4 presents the 2-D and 3-D streamlines of the cooling steam in the front and rear cooling cavity and the cascade channel. It can be deduced that in the front cooling steam chamber of the wheel, with the change in the flow cross-section, numerous vortices are generated in the process of cooling steam flow, and the vortex generation area corresponds to the low speed region. The vortex not only played an important role in cooling the surface of the wheel but also prevented the catalyst particles in the flue gas from entering the cooling steam domain. The front cooling steam entered the axial clearance, mixed with the flue gas, and then flowed into the rotating blade channel. Owing to the high speed rotation and acceleration of

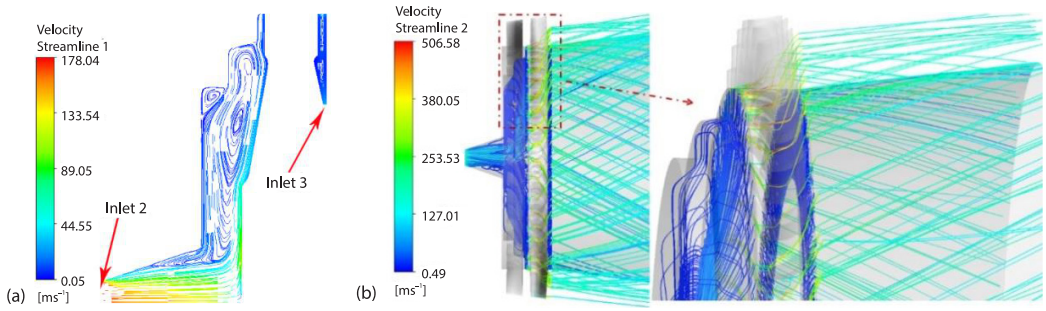

Figure 4. Meridian and 3-D streamlines of the cooling and sealing steam; (a) meridian streamlines and (b) 3-D streamlines

the rotating blades, the streamline of the cooling steam is radially shifted when the steam flows through the rotating blade channel, as illustrated in fig. 4(b). The steam from the rear cooling chamber (sealing steam) enters the mixing annular region, mixes with the flue gas, and flows out mainly along the bottom surface of the exhaust casing. Evidently, the cooling steam from the front cooling chamber has a more significant influence on the main stream of the flue gas turbine than that of the sealing steam.

The mixing of cooling steam and flue gas is indicated by the contours of the mass fraction distribution of gas in the inlet and outlet sections of the rotating blades, as shown in fig. 5. In the 0.05-0.1 span region of the inlet section of the rotating blades, the cooling steam accounted for 70% of the total mass of working fluid, while the remaining region was occupied by the flue gas. As the mixture of flue gas and cooling steam moved downstream, the distribution of cooling steam along the blade height direction tended to be uniform under the combined action of the radial motion of cooling steam and the rotational force of the rotor. The maximum mass fraction of cooling steam in the local area of the rotating blade exit section was approximately 8%.

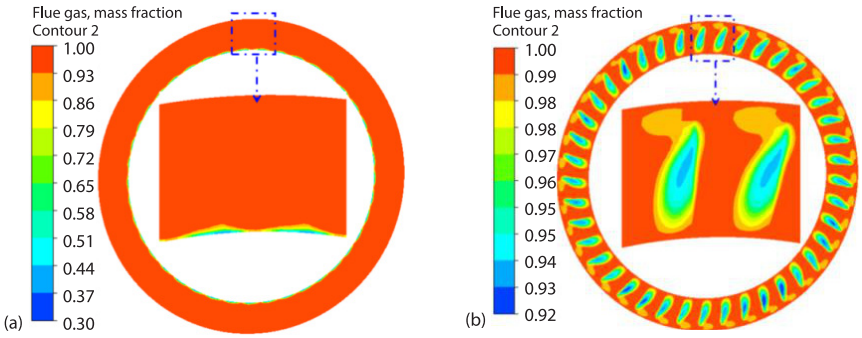

Figure 5. Contours of the flue gas mass fraction distribution under the design condition; (a) rotor inlet section and (b) rotor outlet section

Owing to the impingement and mixing of the cooling steam, the normal flow state of the main flue gas stream was disturbed. Figure 6 presents the limiting streamlines on the surfaces of the stator and rotor blades under the design condition. In the figure, PS denotes pressure surface, and SS denotes suction surface. Evidently, the surface streamline trajectory of the stator is smooth, and the flue gas-flows downstream primarily in the axial direction. By contrast, the streamlines on the pressure and suction surfaces of the rotor blades exhibit radial

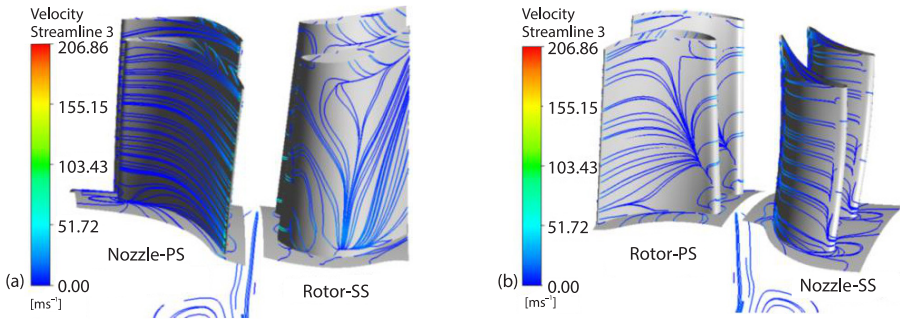

Figure 6. Limiting streamlines on the stator and rotor surfaces under the design conditions; (a) nozzle-PS and rotor-SS and (b) nozzle-SS and rotor-PS

motion, which is closely related to the existence of a radial pressure gradient on the rotor blade surface and the radial impact of the cooling steam from axial clearance. The radial motion of the limiting streamlines on the rotor blade surface indicates that a secondary vortex flow exists in the cascade of rotor blades, and the impact and mixing of the wheel cooling steam enhances the strength of the secondary flow.

These observations indicate that the mixing flow of the flue gas and cooling steam in the entire flow channel of the flue gas turbine is complex. In addition the local resistance loss and friction loss, wake loss, shock wave loss, separation loss, secondary flow loss, and steam-gas mixing loss occur in the flow passages of the turbine. These losses reduce the effective work energy of the turbine. The aerodynamic performance of the flue gas turbine can be expressed in terms of the isentropic efficiency, which is defined as the ratio of the actual enthalpy drop of the expanding fluid from the inlet to the outlet to the ideal enthalpy drop of the isentropic expansion process from inlet to the outlet. Numerical results indicate that the isentropic efficiency of the flue gas turbine is 78.74% under the design conditions.

Influence of cooling steam flow on the aerodynamic performance of the flue gas turbine

To investigate the effect of the wheel cooling steam on the aerodynamic performance of the flue gas turbine, the effect of altering the cooling steam flow rate (Inlet 2) on the aerodynamic performance of the flue gas turbine was investigated with the other conditions held constant. The cooling steam inlet parameters under different conditions are listed in tab. 3, where Q_{cs} and T_{cs} represent the cooling steam inlet flow rate and temperature, respectively, and $\overline{Q}_{cs}$ represents the dimensionless steam flow rate, which is defined as the ratio of the cooling steam flow rate of Inlet 2 under the calculation conditions to the cooling steam flow rate of Inlet 2 under the design conditions. The $\overline{Q}_{cs}$ is adopted to distinguish the different calculation conditions.

Table 3. Cooling steam inlet parameters under different calculation conditions

Conditions	Q_{cs} at Inlet 2 [kgs^{-1}]	T_{cs} at Inlet 2 [K]	Q_{cs} at Inlet 3 [kgs^{-1}]	T_{cs} at Inlet 3 [K]
$\overline{Q}_{cs}$ = 2.0	0.278	523	0.0556	523
$\overline{Q}_{cs}$ = 1.6	0.2224	523	0.0556	523
$\overline{Q}_{cs}$ = 1.3	0.139	523	0.0556	523
$\overline{Q}_{cs}$ = 1.0	0.139	523	0.0556	523
$\overline{Q}_{cs}$ = 0.6	0.0834	523	0.0556	523

Figures 7 and 8 present the contours of the static entropy at the rotor inlet and outlet, respectively. Evidently, the patterns of the static entropy distribution in the inlet and outlet sections of the rotating blade are almost identical for different cooling steam flow rates. The maximum value of the static entropy for the rotating blade inlet section occurred in the low blade span region near the root of the blade, whereas the maximum value of the static entropy of the rotating blade outlet section was observed in the middle- and high blade span regions. As indicated by the contours of the gas mass fraction distribution of the rotor inlet and outlet sections under the design condition in fig. 5, the static entropy and gas mass distributions of the same sections have a high degree of similarity. This indicates that in the flow passages of the rotating blade, the mixing loss of the cooling steam and flue gas and the enhanced secondary flow loss significantly affected the entropy increment of the working fluid. In addition, as is evident from figs. 7 and 8, the static entropy gradient in the inlet section of the rotor blade cascade is larger than that in the outlet section of the rotor blade cascade for the same cooling steam flow rate,

indicating that the mixing and secondary flow losses generated by the cooling steam after it enters the main gas domain gradually decreases along the flow direction.

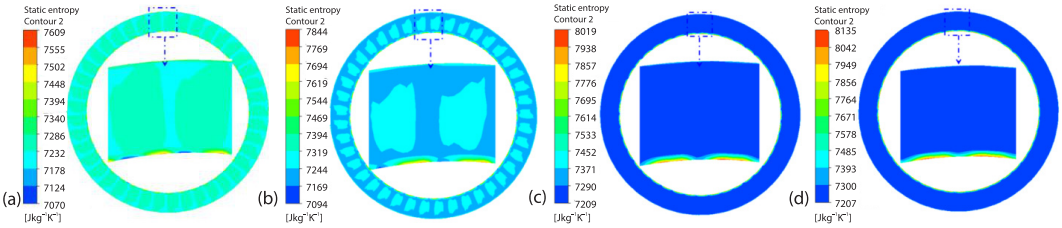

Figure 7. Contours of the static entropy at the rotor inlet under different $\bar{Q}_{cs}$; (a) $\bar{Q}_{cs}$ = 0.6, (b) $\bar{Q}_{cs}$ = 1.0, (c) $\bar{Q}_{cs}$ = 1.6, and (d) $\bar{Q}_{cs}$ = 2.0

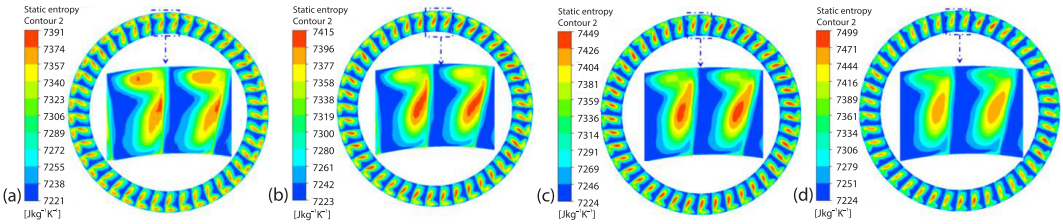

Figure 8. Contours of the static entropy at the rotor outlet under different $\bar{Q}_{cs}$; (a) $\bar{Q}_{cs}$ = 0.6, (b) $\bar{Q}_{cs}$ = 1.0, (c) $\bar{Q}_{cs}$ = 1.6, and (d) $\bar{Q}_{cs}$ = 2.0

Figure 9 presents the distribution of the mass-flow averaged static entropy along the axial direction. The horizontal co-ordinates in the figure represent the dimensionless axial co-ordinates. Here, 0-1, 1-2, 2-3, and 3-4 represent the nozzle, axial clearance, rotor, and mixing annular region domains, respectively. Evidently, the distribution patterns of static entropy along the axial direction are almost identical for different cooling steam flow rates. This indicates that the types and locations of the irreversible flow losses in the entire flue gas turbine flow channel are identical for different steam flow rates. As the cooling steam flow rate increased, the static entropy distribution in the stator cascade remained constant, whereas the static entropy in the axial clearance, rotor cascade, and mixing annular region domains increased significantly. This is because the stator cascade domain was upstream of the cooling steam entry port, and the change in the cooling steam flow rate had no effect on the irreversible flow losses in the stator cascade. However, as the cooling steam flow rate increased, the irreversible flow losses, such as mixing and secondary flow losses in the axial clearance, rotor, and mixing annular region domains increased, increasing the static entropy of the aforementioned fluid domains.

Figure 10 presents the turbine isentropic efficiency with respect to the cooling steam flow rate. The horizontal co-ordinates in the figure represent the dimensionless cooling steam flow rates. As indicated by figs. 9 and 10, as the front cooling steam flow rate increased, the flue gas-steam mixing and secondary flow losses caused by the cooling steam increased, and the entropy increment in the flue gas turbine cascade increased, reducing the isentropic efficiency of the flue gas turbine. When the dimensionless cooling steam flow rate decreased from 1 to 0.6, the isentropic efficiency of the flue gas turbine increased by approximately 0.9%. When the dimensionless cooling steam flow rate increased from 1 to 2, the isentropic efficiency of the flue gas turbine decreased by 0.42%. Evidently, reducing the cooling steam flow rate significantly improves the aerodynamic performance of the flue gas turbine, provided that the turbine wheel is at the normal operating temperature.

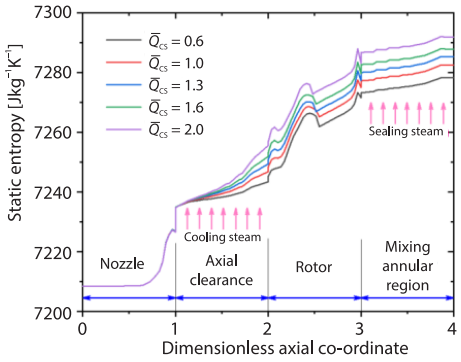

Figure 9. Distribution of the average static entropy along the axial direction

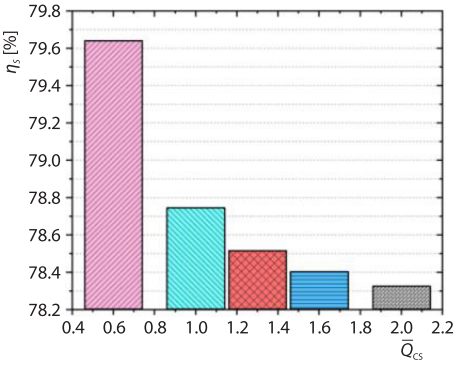

Figure 10. Turbine isentropic efficiency with respect to the cooling steam flow rate

Particle motion and erosion characteristics in flue gas turbine cascades

The motion and erosion behavior of the particles within the complex flow field were systematically investigated in this section. The catalyst particles cannot enter the cooling steam domain, owing to the positive pressure gradient resulting from the flow of cooling steam to the main flue gas and the blockage of the steam vortex at the top of the front cooling steam domain. Figure 11 presents the particle trajectories in the turbine cascade. Evidently, the acceleration characteristics of the flue gas on the particles are closely related to the particle size. The maximum velocity of the catalyst particles decreased from 820-360 m/s as the particle size increased from 1-30 μm. As is evident from figs. 11(a)-11(c) and fig. 3, the location of the maximum particle velocity (axial clearance between stators and rotating blades) is downstream of the location of the maximum air-flow velocity (nozzle outlet), indicating that the acceleration of particles by the air-flow exhibits a lag. In addition, comparing the four plots in fig. 11 reveals that the maximum velocity for 30 μm particles was generated in the exhaust casing, which differs from that for smaller particles. This indicates that for large particles, the rotational force generated by the high speed rotation of the rotor has a stronger accelerating effect on the particles than the air-flow traction.

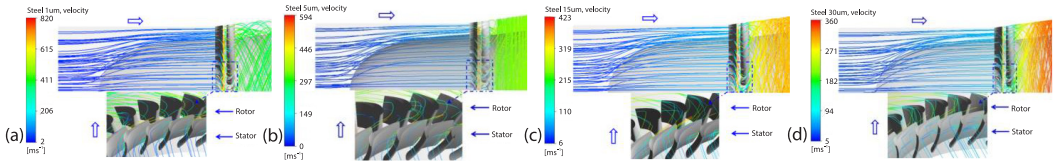

Figure 11. Particle trajectories for different particle sizes; (a) 1 μm, (b) 5 μm (c) 15 μm, and (d) 30 μm

Figure 12 shows the erosion rate density on the surfaces of the stator and rotor blades. Because the flue gas turbine considered in this study had a full-circumferential intake structure, the trajectories of catalyst particles in different circumferential turbine cascades were similar, and the distributions of the erosion on the stator and rotor blades were almost identical. Therefore, only the erosion rate contours of the surfaces of the stator and rotor blades located directly above the rotor center are presented in this paper. As is evident from figs. 11 and 12, the probability of 1 μm and submicro particles hitting the flow channel is negligible; therefore, the erosion on the stator and rotor can be neglected. As the particle size increased, the position

of the catalyst particles hitting the pressure surface of the stator moved upstream, fig. 11, and the resulting erosion area moved toward the leading edge of the stator, fig. 12(a). As indicated by the particle trajectory in fig. 11, the maximum velocities of the particles occurred in the clearance between the stator and rotor or exhaust pipe, and the velocities of the particles directly impacting the stator pressure surface were low, consequently, the degree erosion of the turbine stators due to the catalyst particles was relatively low.

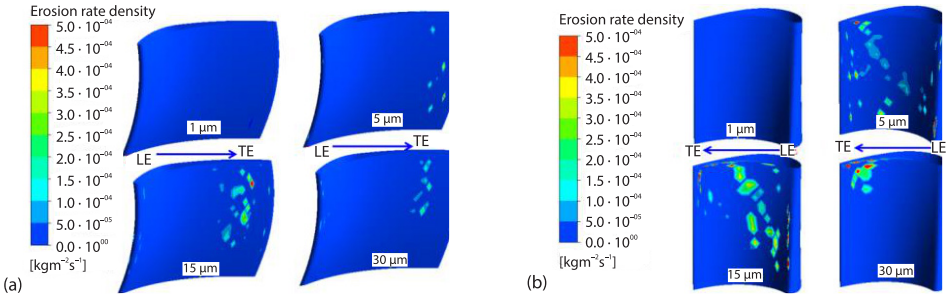

Figure 12. Contours of erosion rate density (LE – leading edge and TE – trailing edge); (a) nozzle and (b) rotor

Compared with the stators, the catalyst particles caused more severe erosion on the rotor blade. As is evident from fig. 12(b), 5 μm particles cause localized wear on the roots of the rotor blade, and larger particles (15 and 30 μm) cause severe erosion on the rotor leading edge and the blade-tip trailing edge on the pressure surface. The contributions of particles of different sizes to the erosion of the rotor are indicated by the erosion rate density statistics for different blade span sections in fig. 13. Evidently, the erosion rates of the leading and trailing edges of the rotor are higher than those at the other streamwise locations of the rotor in different blade span sections, which is consistent with the actual erosion profiles of the rotor blades obtained in the investigation. Additionally, for the root region of the rotor, 0.05 span in fig. 13(a), the erosion effect of particles with sizes of 1-5 μm is significant. Careful analysis indicates that although the probability of 1-5 μm particles directly impacting the surface of the rotor cascade is low, these particles are easily carried by the secondary flow in the turbine cascade, causing repeated grinding in the local region of the blade root. Figure 14 presents the trajectories of 1 and 5 μm particles in the rotor cascade. The results are consistent with the direction of the vortex motion corresponding to the limit streamline on the surface of the rotor presented in fig. 6, confirming that the local erosion near the root of the rotor cascade is caused by the grinding of 1-5 μm particles following the vortex motion of the secondary flow. The position of 10-20 μm particles impacting the rotor cascade moved radially upward, figs. 13(c) and 13(d) under the

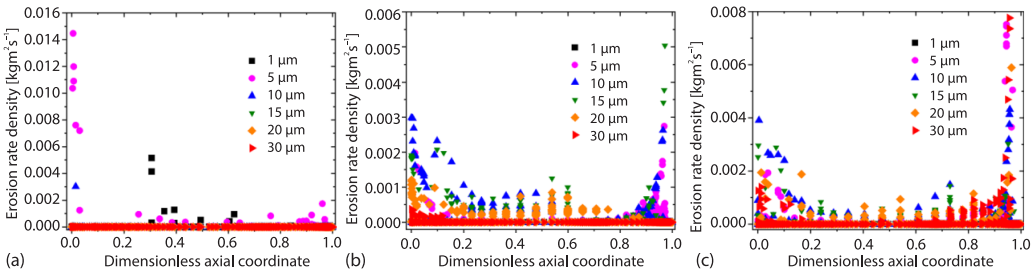

Figure 13. Erosion rate density for different spans of the rotor blades; (a) 0.05 span, (b) 0.5 span, and (c) 0.95 span

action of centrifugal force. Consequently, in the midspan section, the contribution of 10-20 μm particles to the blade erosion was relatively large. With a further increase in the particle size, the radial displacement of the particles increased, causing more severe erosion in the rotor blade tip region. Therefore, in the 0.95 blade span section, fig. 13(c), the proportion of erosion caused by 20-30 μm particles increased significantly.

Figure 15 presents a comparison between the predicted and actual erosion erosion morphologies [1] of the rotor blade. Evidently, the predicted results are consistent with the actual erosion morphology of the flue gas turbine, validating the reliability of the numerical simulation method adopted in this study. The simulation results indicate that the erosion notch at the trailing edge of the rotor blade tip and the wall roughness at the rotor leading edge are caused by the high speed impact of the large (>10 μm) catalyst particles. By contrast, the localized erosion in the root area of the rotor blade is caused by the long-term grinding of small (1-5 μm) particles. To control the high speed impact of catalyst particles on the leading and trailing edges of the rotor blade, the particle separation efficiency of the upstream cyclone of the flue gas turbine must be strictly controlled to minimize the number of large particles entering the flue gas turbine. Because it is difficult to separate small (<5 μm) particles, their erosion intensity in the root region of the flue gas turbine rotor blade must be reduced by controlling the intensity of the secondary flow vortex. Specifically, the generation and development of the secondary flow in the turbine cascade can be controlled by optimizing the blade structure (*e.g.*, changing the blade loading characteristics). Moreover, the observations presented in sections *Aerodynamic loss analysis of the flue gas turbine under design condition* and section *Influence of cooling steam floe on the aerodynamic performance of the flue gas turbine* indicate that the radial impact and mixing of excess cooling steam from the axial clearance with the main flow of flue gas enhance the intensity of secondary flow in the rotor cascade. Therefore, to reduce the degree of erosion at the root of the rotor, the flow of cooling steam in front of the wheel must be reduced while optimizing the blade profile, which reduces the carrying effect of the secondary flow vortex of the turbine cascade on small particles.

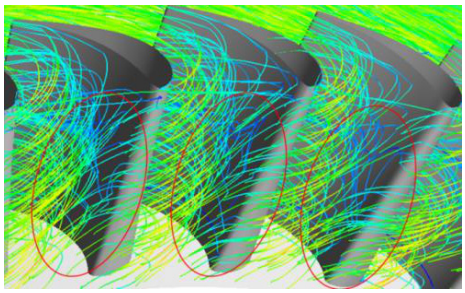

Figure 14. Trajectories of 1 and 5 μm particles in the rotor cascade

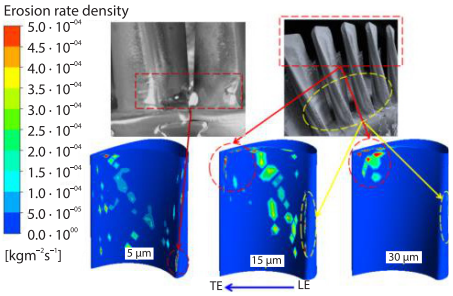

Figure 15. Erosion prediction and the actual erosion morphology of the rotor blade

Conclusion

The aerodynamic loss characteristics of the flue gas-steam mixtures and particle erosion mechanism in the flue gas turbine cascade under design and non-design conditions have been researched in this paper. The following conclusions are drawn. The radial inflow of wheel cooling steam from the axial clearance between the stator and rotor exerted a radial impact and mixing effect on the mainstream flue gas, enhancing the generation and development of the secondary flow vortex in the rotor cascade. The mixing loss generated by the cooling steam af-

ter it entered the main gas domain gradually decreased along the flow direction. The isentropic efficiency of the flue gas turbine under the design condition was 78.74%. As the cooling steam flow rate at the front of the wheel increased, the flue gas-steam mixing and secondary flow losses increased, reducing the isentropic efficiency of the flue gas turbine. When the dimensionless cooling steam flow rate increases from 1 to 2, the isentropic efficiency of the flue gas turbine decreased by 0.42%. The erosion rates of the leading and trailing edges of the rotor are higher than those at other streamwise locations. The erosion of the rotor leading edge and the blade-tip trailing edge was found to be caused by the high speed impact of large (>10 μm) catalyst particles, and the local erosion in the root area of the rotor resulted from the repeated grinding of small (1-5 μm) particles carried by the secondary flow. For different erosion mechanisms, corresponding measures are provided.

Acknowledgment

The authors thank the National Natural Science Foundation of China (NSFC) (No. 52076173), the China Postdoctoral Science Foundation (No. 2020M680157), and the Fundamental Research Fund of the Central Universities (No. sxxj032020009) for funding.

Nomenclature

$A_f(T)$ – temperature function in eq. (8), [–]
$B(\beta)$ – impingement angle function in eq. (8), [–]
e_T – normal velocity restitution coefficients, [–]
e_N – tangential velocity restitution coefficients, [–]
E_m – material erosion rate, [kgm^{2}s^{-1}]
Ma – Mach number of gas phase, [–]
Q_{cs} – mass-flow at inlet of cooling steam, [kgs^{-1}]
$\overline{Q}_{cs}$ – dimensionless steam flow, [–]
Q_{out} – mass-flow at outlet of main flue gas, [kgs^{-1}]
T – surface temperature of target in the test, [K]
T_{cs} – temperature at inlet of cooling steam , [K]
T_{out} – temperature at outlet of main flue gas, [K]
V – particle impingement velocity [m·s-1],
$V_{10\mu m}$ – maximum speed of 10 μm particle, [ms^{-1}]

Greek symbols

β – angle of particle incidence in radian, [–]
η_s – isentropic efficiency of flue gas turbine, [–]
Γ_i – molecular diffusivity, [m^{2}s–1]
ρ – density of gas fluid, [kgm^3]
λ – thermal conductivity, [Wm^{-1}K^{-1}]

Acronym

OEM – original equipment manufacture

References

[1] Maceli, N., *et al.*, An Industrial Methodology for Erosion Analysis of FCC Expander Blades, *Proceedings*, ASME Turbo Expo 2020, Virtual, Online, 2020
[2] Chang, J., *et al.*, Hydrodynamic Modelling of an Industrial Turbulent Fluidized Bed Reactor with FCC Particles, *Powder Technology*, *304* (2016), Dec., pp. 134-142
[3] Xiong H. Y., *et al*., Vibration Fault Signal Analysis and Diagnosis of Flue Gas Turbine, *Engineering Failure Analysis*, *134* (2022), 105981
[4] Liu, G. K., *et al.*, Simulation Study on the Effect of Flue Gas on Flow Field and Rotor Stress in Gas Turbines, *Energies*, *14* (2021), 19, 6135
[5] Xu, W. W., *et al*., Modelling and Numerical Analysis of the Effect of Blade Roughness on Particle Deposition in a Flue Gas Turbine, *Powder Technology*, *347* (2019), Apr., pp. 59-65
[6] Gao, X. W., *et al.*, Research Progress of Catalysts Fouling in Flue Gas Turbines Used in Catalytic Cracking Unit, *China Powder Science and Technology*, *21* (2015), 6, pp. 25-32
[7] Lin, G. Q., *et al*., Stress and strain Analysis of First Stage Rotating Blades of Flue Gas Turbine Blades, *Applied Mechanics and Materials*, *130-134* (2012), Oct., pp. 691-695
[8] Zheng, L. J., *et al.*, Blades Fracture Failure Analysis of a Certain Flue Gas Turbine, *Petro-Chemical Equipment*, *47* (2018), 6, pp. 74-79
[9] Sun, J. G., *et al*., A Study into High-Temp Protective Coatings for Flue Gas Turbine Blades, *Sino-Global Energy*, *13* (2008), pp. 37-39
[10] Min, X. B., *et al*., Anatomy and Analysis of the Great Wall No. 1 Coating on The Rotor Blades of the in-Service Flue Gas Turbine, *Proceedings*, 2003 China Shanghai Hard Surface Technology Academic Exchange Conference, Shanghai, China, 2003

[11] Liu, W. C., Study on the Technology and Properties of Detonation Gun Sprayed Cr_3C_2-NiCr Coatings, M. Sc. thesis, Lanzhou University of Technology, Lanzhou, China, 2019
[12] Cai, L. X., *et al*., New Features of Solid Particle Erosion Damage of Control Stage Blades in Supercritical Steam Turbine, Proc. IMechE – Part A, *Journal of Power and Energy*, *230* (2016), 1, pp. 76-85
[13] Bennett, E., *et al.*, Predicting Turbomachinery Erosion Rates, *ANSYS Advantage*, *2* (2011), 5, pp. 31-33
[14] Carbonetto, B., *et al*., Advances in Erosion Prediction of Axial Flow Expanders, *Proceedings*, 28th Turbomachinery Symposium, Texas A&M University, Colege Station, Tex., USA, 1999
[15] Du, Y. P., *et al.*, Catalyst Fines Behavior among FCC Flue Gas Turbine Blade Rows-Effect of Gaseous Phase Flow Field Distribution, *Chemical Engineering*, *40* (2012), 7, pp. 57-60
[16] Du, Y. P., *et al.*, Catalyst Fines Behavior among FCC Flue Gas Turbine Blade Rows-Erosion and Fouling on Blades, *Chemical Engineering*, *40* (2012), 9, pp. 52-55
[17] Gandhi, N., *et al*., Reliability Improvement in FCC Hot Gas Expander Using CFD Modelling, *Proceedings*, 16th International Symposium on Transport Phenomena and Dynamics of Rotating Machinery, Honolulu, Hi., USA, 2016
[18] Cai, L. X., *et al.*, Gas-Particle Flows and Erosion Characteristic of Large Capacity Dry Top Gas Pressure Recovery Turbine, *Energy*, *120* (2017), Feb., pp. 498-506
[19] Cai, L. X., *et al*., The Influence of Nozzle Chamber Structure and Partial-Arc Admission on The Erosion Characteristics of Solid Particles in the Control Stage of a Supercritical Steam Turbine, *Energy*, *82* (2015), Mar., pp. 341-352
[20] Chen, S. F., *et al*., Model of Particle Deposition and Adhesion on Blade Surface of Flue Gas Turbine, *The Chinese Journal of Process Engineering*, *18* (2018), 3, pp. 447-453
[21] Fei, D., *et al.*, Analysis of Scaling Reason and Simulation of Flow Field of FCCU Power Recovery Expander, M. Sc. thesis, East China University of Science and Technology, Shanghai, China, 2015
[22] Wang, Y., *et al*., Experiment Research on Scaling Mechanism of Catalyst in Fluid Catalytic Cracking Flue Gas Turbine, *China Powder Science and Technology*, *22* (2016), 1, pp. 92-96
[23] Fei, D., *et al.*, Analysis of Mechanism of Fouling Increase on Blades of FCCU Power Recovery Expander, *CIESC Journal*, *66* (2015), 1, pp. 79-85
[24] Cai, L. X., *et al*., Experimental and Numerical Studies on Rebound Characteristics of Non-Spherical Particles Impacting on Stainless-Steel at High Temperature, *Powder Technology*, *381* (2021), Mar., pp. 110-121
[25] Wang, S. S., *et al*., Influence of the Inlet Channel Flow of a Steam Turbine on Solid Particle Erosion of the Control Stage Nozzles, Proc. IMechE – Part A, *Journal of Power and Energy*, *226* (2012), 5, pp. 636-649

Paper submitted: November 25, 2022
Paper revised: February 28, 2023
Paper accepted: March 12, 2023